Journal of
Materials Chemistry C

PAPER

View Article Online
View Journal | View Issue

Open Access Article. Published on 30 October 2019. Downloaded on 10/20/2025 7:21:48 PM.
This article is licensed under a Creative Commons Attribution 3.0 Unported Licence.

Check for updates

Cite this: J. Mater. Chem. C, 2019, 7, 15049

Investigation on voltage loss in organic triplet photovoltaic devices based on Ir complexes†

Yingzhi Jin,‡[a] Jie Xue,‡[b] Juan Qiao *[b] and Fengling Zhang *[a]

Received 5th September 2019,
Accepted 29th October 2019

DOI: 10.1039/c9tc04914b

rsc.li/materials-c

Voltage losses in singlet material-based organic photovoltaic devices (OPVs) have been intensively studied, whereas, only a few investigations on triplet material-based OPVs (T-OPVs) are reported. To investigate the voltage loss in T-OPVs, two homoleptic iridium(III) complexes based on extended π-conjugated benzo[*g*]phthalazine ligands, $Ir(Ftbpa)_3$ and $Ir(FOtbpa)_3$, are synthesized as sole electron donors. T-OPVs are fabricated by mixing two donors with phenyl-C_{71}-butyric acid methyl ester ($PC_{71}BM$) as an electron acceptor. Insertion of oxygen-bridges as flexible inert δ-spacers in $Ir(FOtbpa)_3$ has slightly elevated both the lowest unoccupied molecular orbital and the highest occupied molecular orbital levels compared to those of $Ir(Ftbpa)_3$, which results in a lower charge transfer (CT) state energy (E_{CT}) for $Ir(FOtbpa)_3$-based devices. However, a higher V_{oc} (0.88 V) is observed for $Ir(FOtbpa)_3$-based devices than those of $Ir(Ftbpa)_3$ (0.80 V). To understand the above result, the morphologies of the two blend films are studied, which excludes the influence of morphology. Furthermore, radiative and non-radiative recombination in two devices is quantitatively investigated, which suggests that a higher V_{oc} can be attributed to reduced radiative and non-radiative recombination loss for the $Ir(FOtbpa)_3$-based devices.

Introduction

Solar energy is considered to be a promising renewable energy source to address the increasing worldwide energy demands. In particular, solution processed bulk-heterojunction (BHJ) organic photovoltaic devices (OPVs) have been identified as promising candidates because of their potential in low-cost, large-area, light-weight and flexible productions. To date, power conversion efficiencies (PCE) over 15% have been achieved for single junction OPVs with the emergence of non-fullerene acceptors,[1,2] which makes OPVs feasible for industrialization. The voltage losses in OPVs have been regarded as the major challenge remaining to further improve the PCE comparable with inorganic or hybrid perovskite PVs.

The open-circuit voltage (V_{oc}) in OPVs is proportional to the energy of the charge transfer (CT) state (E_{CT}) between the donor and acceptor.[3] It has been found that the energetic difference between the highest occupied molecular orbital (HOMO) of the donor and the lowest unoccupied molecular orbital (LUMO) of the acceptor is roughly equal to E_{CT}.[4–6] Therefore, many reports are focused on increasing the V_{oc} through increasing E_{CT} by minimizing the energetic offset between donors and acceptors.[7–9] Increasing E_{CT} will however lead to a small driving force (defined as the energy difference between optical gap of the neat donor or acceptor and E_{CT}) for exciton dissociating to free charges. Generally, fullerene based OPVs tend to show low PCEs with small driving forces (<0.3 eV), whereas, a reasonably high IQE (>85%) was obtained for P3TI:$PC_{71}BM$ blends with a small driving force of 0.1 eV.[10] Recently, non-fullerene based OPVs have exhibited efficient exciton dissociation despite a negligible driving force.[11–14] Furthermore, the voltage loss between E_{CT}/q to V_{oc} is due to radiative and non-radiative recombination. An empirical relation of $V_{oc} = \frac{E_{CT}}{q} - 0.6$ V, has been found for fullerene based OPVs, of which radiative recombination at donor/acceptor interfaces *via* the CT state causes ~0.25 V loss and non-radiative recombination causes ~0.35 V loss.[3,15] Thus, reducing recombination losses is another important strategy to obtain a high V_{oc}.[16] It was reported that decreasing the donor/acceptor interfacial area is an effective way to reduce voltage losses.[17] Therefore, high V_{oc} can be achieved for organic materials with long exciton diffusion lengths, which will enable a reduced optimum interfacial area. Furthermore, reducing non-radiative recombination losses (<0.3 V) enabled high V_{oc} for materials with high photoluminescence (PL) yields, which have also been reported.[18,19]

At present, the photo-induced charges mainly originate from singlet exciton dissociation in high performance OPVs.

[a] Department of Physics, Chemistry and Biology, Linköping University, Linköping SE-58183, Sweden. E-mail: fengling.zhang@liu.se
[b] Key Lab of Organic Optoelectronics and Molecular Engineering of Ministry of Education, Department of Chemistry, Tsinghua University, Beijing 100084, China. E-mail: qjuan@mail.tsinghua.edu.cn

† Electronic supplementary information (ESI) available. CCDC 1916919. For ESI and crystallographic data in CIF or other electronic format see DOI: 10.1039/c9tc04914b

‡ These authors contributed equally to this work.

Open Access Article. Published on 30 October 2019. Downloaded on 10/20/2025 7:21:48 PM.
This article is licensed under a Creative Commons Attribution 3.0 Unported Licence.

Triplet excitons, which have longer lifetimes or diffusion lengths than singlets, may provide a favorable approach to increase the photocurrent of OPVs due to the forbidden nature of recombination from the triplet state.[20,21] In addition, the long diffusion lengths are beneficial to have large domains with decreased interfaces, which will further improve V_{oc}.[17] In general, the excitons generated by absorbing photons in organic materials are singlet due to the selection rule in the electronic dipole transition processes.[22] The triplet excitons can be obtained by flipping the spin orientation of singlet excitons through the effective intersystem crossing (ISC) or by bimolecular singlet fission.[23,24] Enlarging spin–orbit coupling (SOC) by chemically or physically introducing heavy atoms into the conjugated materials has been proposed to enhance ISC rate.[25–27] So far, some research studies have been done on triplet material-based OPVs (T-OPVs)[28–31] and the highest PCE for small-molecule Ir complexes is 3.81%.[32] However, the voltage losses in T-OPVs were rarely investigated.[33] In terms of recombination losses, the long exciton diffusion lengths and high emissive properties of triplet materials are beneficial for large V_{oc}.

Here, we therefore investigate the voltage losses in T-OPVs *via* radiative and non-radiative recombination losses by employing highly sensitive external quantum efficiency and electroluminescence (EL) measurements. Two homoleptic iridium (Ir) complexes, tris(1-(2,4-bis(trifluoromethyl)phenyl)-4-(thiophen-2-yl)benzo[*g*]-phthalazine) Ir(III) ((Ir(Ftbpa)$_3$) and tris(1-(2,5-bis(trifluoromethyl)-phenoxy)-4-(thiophen-2-yl)benzo[*g*]phthalazine) Ir(III) (Ir(FOtbpa)$_3$), are designed as electron donors and phenyl-C_{71}-butyric acid methyl ester ($PC_{71}BM$) is used as the electron acceptor. OPVs based on Ir(Ftbpa)$_3$ and Ir(FOtbpa)$_3$ donors exhibit PCEs of 3.17% and 3.56%, which are decent performances regarding the studies on T-OPVs to date, and also showed great enhancement compared to poor photovoltaic performance of the 1-chloro-4-(thiophen-2-yl)benzo[*g*]phthalazine (Ftbpa) (0.001%) and 1-(2,5-bis(trifluoromethyl)phenoxy)-4-(thiophen-2-yl)benzo[*g*]phthalazine (FOtbpa) (0.007%) ligands as donors. More importantly, a higher V_{oc} is achieved for Ir(FOtbpa)$_3$-based devices despite a lower E_{CT}, which is attributed to the reduced radiative and non-radiative recombination loss.

Experimental section

Synthesis and characterization

All commercially available reagents and chemicals were used without further purification. All reactions involving air-sensitive reagents were carried out under an atmosphere of nitrogen.

1-Chloro-4-(thiophen-2-yl)benzo[*g*]phthalazine, Ftbpa and Ir(Ftbpa)$_3$ was synthesized according to the literature reports.[34]

Synthesis of FOtbpa. To a 50 mL round-bottom flask, 1-chloro-4-(thiophen-2-yl)benzo[*g*]phthalazine (1.184 g, 4 mmol), 2,5-bis-(trifluoromethyl)phenol (1.20 g, 5.2 mmol), potassium carbonate (1.79 g, 13 mmol), and *N*,*N*-dimethylformamide (20 mL) were added. The mixture was heated to 110 °C under a nitrogen atmosphere for 5 h. After cooling to room temperature, the mixture was poured into 100 mL water. The precipitate was then collected by filtration, and washed with water and dried in a vacuum. The crude product was purified by column chromatography on silica gel (hexane/dichloromethane = 1 : 1, v/v). Then, the crude product was recrystallized from dichloromethane/hexane to give FOtbpa as a yellow solid. Yield: 82%. ^{1}H NMR (600 MHz, $CDCl_3$): δ 9.10 (s, 1H), 9.07 (s, 1H), 8.27 (d, J = 7.8 Hz, 1H), 8.20 (d, J = 7.8 Hz, 1H), 7.95 (s, 1H), 7.91 (d, J = 8.2 Hz, 1H), 7.86 (d, J = 3.3 Hz, 1H), 7.82–7.75 (m, 2H), 7.67 (d, J = 8.3 Hz, 1H), 7.64 (d, J = 4.9 Hz, 1H), 7.32 (t, J = 4.3 Hz, 1H). HRMS (ESI$^+$) *m*/*z*: calcd for $C_{24}H_{13}F_6N_2OS^+$ $[M + H]^+$: 491.0653, found: 491.0692.

Synthesis of Ir(FOtbpa)$_3$. A mixture of FOtbpa (1.62 g, 3.3 mmol), $IrCl_3{\cdot}3H_2O$ (0.35 g, 1 mmol), 2-methoxyethanol (30 mL) and distilled water (10 mL) was stirred at 110 °C for 24 h under nitrogen. After cooling to room temperature, 50 mL of distilled water was added and the precipitate was filtered off and washed with water, ethanol and hexane. The crude product was purified by column chromatography over aluminum oxide using hexane/dichloromethane (2 : 1, v/v) as the eluent to give Ir(FOtbpa)$_3$ as a black solid. Yield: 25%. ^{1}H NMR (600 MHz, $CDCl_3$): δ 9.16 (s, 3H), 8.69 (s, 3H), 8.28 (d, J = 8.3 Hz, 3H), 8.17 (d, J = 8.2 Hz, 3H), 7.82–7.78 (m, 3H), 7.78–7.73 (m, 3H), 7.34 (d, J = 4.2 Hz, 3H), 7.12 (s, 3H), 6.64 (d, J = 4.7 Hz, 3H), 6.54 (d, J = 8.2 Hz, 3H), 5.71 (d, J = 8.1 Hz, 3H). HRMS (MALDI-TOF) *m*/*z*: calcd for $C_{72}H_{33}F_{18}IrN_6O_3S_3^+$ $[M]^+$: 1660.1118, found: 1660.2736. Elemental analysis calcd for $C_{72}H_{33}F_{18}IrN_6O_3S_3$: C, 52.08; H, 2.00; N, 5.06; found: C, 52.08; H, 2.28; N, 5.19.

Characterization

^{1}H NMR spectra were measured using a JEOLAL-600 MHz spectrometer at ambient temperature. High resolution mass spectra were recorded using a Thermo-Electron Corporation Finnigan LTQ mass spectrometer (ESI-MS) and LCMS-IT/TOF (HRMS). The laser desorption ionization time-of flight mass spectrometry (LDI-TOF-MS) data were obtained using a Shimadzu AXIMA Performance MALDI-TOF instrument in both positive and negative detection modes with an applied voltage of 25 kV between the target and the aperture of the time-of-flight analyzer. Elemental analysis was performed using a flash EA 1112 spectrometer. The single crystal of Ir(FObpa)$_3$ was obtained from the diffusion of a chloroform/hexane mixture. The low temperature (104.6 K) single-crystals X-ray experiments were performed using a Rigaku RAXIS-SPIDER IP diffractometer with graphite-monochromatized MoKα radiation (λ = 0.71073 Å). Data collection and reduction, cell refinement, and experiential absorption correction were performed with the Rigaku RAPID AUTO software package (Rigaku, 1998, Version 2.30). CCDC 1916919.† Electrochemical measurement was performed with a Potentiostat/Galvanostat Model 283 (Princeton Applied Research) electrochemical workstation, using Pt as the working electrode, platinum wire as the auxiliary electrode, and a Ag wire as the reference electrode standardized against ferrocene/ferrocenium. The reduction/oxidation potentials were measured in anhydrous DMF solution containing 0.1 M n-Bu_4NPF_6 as the supporting electrolyte at a scan rate of 150 mV s^{-1}.

Device fabrication and characterization

The OPVs were fabricated with the structure of ITO/poly(3,4-ethylenedioxythiophene) doped with poly(styrene-sulfonate) (PEDOT:PSS)/active layer/LiF/Al. The ITO substrates were cleaned

Open Access Article. Published on 30 October 2019. Downloaded on 10/20/2025 7:21:48 PM.
This article is licensed under a Creative Commons Attribution 3.0 Unported Licence.

with detergent and TL-1 ($NH_3:H_2O_2:H_2O = 1:1:5$) for 30 min. PEDOT:PSS was spin-coated on the cleaned ITO substrates followed by annealing at 150 °C for 15 min. The active layers (total 20 mg mL^{-1}) were spin-coated from chloroform (CF) solutions on top of the PEDOT:PSS at 2000 rpm for 40 s in a glovebox filled with N_2. The substrates were moved into a vacuum chamber where 0.6 nm LiF and 90 nm Al were thermally evaporated at a pressure less than 2.0×10^{-4} Pa with a shadow mask to define the active area to be 0.047 cm^2. Hole only devices were fabricated with the structure of ITO/PEDOT:PSS/active layer/MoO_3/Al. Electron only devices were fabricated with the structure of ITO/ZnO/active layer/LiF/Al. The hole or electron mobilities of the BHJ blends were measured using the space-charge-limited current (SCLC) method according to the Murgatroyd law and using eqn (1) to fit the trap-free regions of the dark *J–V* curves from the hole or electron only devices.[35,36]

$$J = \frac{9}{8}\mu_0\varepsilon_r\varepsilon_0\frac{(V - V_{bi})^2}{L^3}\exp\left(\frac{0.89}{kT}\gamma\left(\frac{\sqrt{V - V_{bi}}}{\sqrt{L}}\right)\right) \quad (1)$$

where ε_r is the relative dielectric constant of the blend (3.6), ε_0 is the vacuum permittivity, μ_0 is the zero-field mobility, L is the thickness of the active layer, k is the Boltzmann constant, T is the absolute temperature, and γ is the field enhancement factor.

Current density–voltage (*J–V*) curves are measured by using a Keithley 2400 Source Meter under an illumination of AM 1.5 simulated by a solar simulator (LSH-7320 LED Solar Simulator, Newport). External quantum efficiency (EQE) spectra were obtained using a QE-R system (Enli Technology Co. Ltd, Taiwan). UV-vis absorption spectra were recorded using a PerkinElmer Lambda 900 spectrometer. Photoluminescence (PL) and EL spectra were recorded using an Andor spectrometer (Shamrock sr-303i-B, coupled to a Newton EMCCD silicon detector cooled to −60 °C). For the EL measurements, a Keithley 2400 Source Meter was utilized for applying an external electric field. EQE_{EL} was measured using a homebuilt system using a calibrated large area Si photodiode 1010B from Oriel, a Keithley 2400 Source Meter to provide voltage and record injected current, and a Keithley 485 Picoammeter to measure the emitted light intensity. Fourier-transform photocurrent spectroscopy (FTPS)-EQE was carried out using a Vertex 70 from Bruker optics, equipped with a QTH lamp, quartz beamsplitter and external detector option. A low noise current amplifier (SR570) was used to amplify the photocurrent produced upon illumination of the devices with light modulated by the FTIR. The output voltage of the current amplifier was fed back into the external detector port of the FTIR, Atomic force microscopy (AFM) was performed using a Dimension 3100 system (Digital Instruments/Veeco) with antimony (n) doped silicon cantilevers (SCM-PIT, Veeco) in tapping mode. The active layer thickness was determined using a Veeco Dektak 6M Stylus profilometer.

Results and discussions

The incorporation of the heavy-atom Ir in the organic framework could largely enhance the SOC and lead to an effective ISC rate. As a near-infrared (NIR) phosphorescent material, $Ir(Ftbpa)_3$ possess UV-vis-NIR absorption with edge over 750 nm, long phosphorescent lifetime and good solubility, which makes it a promising donor material for T-OPVs. Although a long excited-state lifetime could be obtained in these noble-metal based dyes, the notorious bimolecular triplet–triplet annihilation between dyes, along with aggregation caused quenching (ACQ) in solid films would enhance the non-radiative rate and thus reduce the excited-state lifetime, which would shorten the exciton diffusion length. The usage of inert substituents could protect and isolate the excitons in the aggregation state and alleviate ACQ. Based on $Ir(Ftbpa)_3$, insertion of oxygen-bridges between the benzo[*g*]-phthalazine moiety and bis(trifluoromethyl)phenyl group generate bis(trifluoromethyl)phenoxy groups as flexible inert δ-spacers to protect the exciton, and thus alleviate the ACQ and maintain long phosphorescent lifetimes for the aggregation states. As a result, $Ir(FOtbpa)_3$ (Fig. 1a) was designed and synthesized with the structure fully characterized by ^1H NMR, high-resolution mass spectrometry, elemental analysis and single-crystal X-ray diffraction measurements.

The single crystals of $Ir(FOtbpa)_3$ were readily grown from a chloroform/methanol mixture. As show in Fig. 1b, the single-crystal X-ray diffraction measurement verified that $Ir(FOtbpa)_3$ possesses a facial configuration around the Ir center. The average

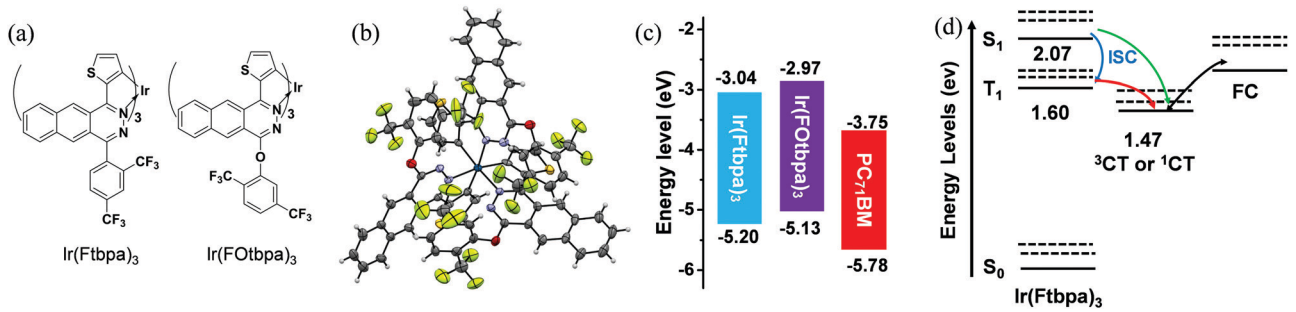

Fig. 1 (a) Chemical structures of $Ir(Ftbpa)_3$ and $Ir(FOtbpa)_3$; (b) single-crystal structure of $Ir(FOtbpa)_3$ with thermal ellipsoids plotted at 50% probability level; (c) energy levels of $Ir(Ftbpa)_3$, $Ir(FOtbpa)_3$ and $PC_{71}BM$; (d) a schematic Jablonski diagram for the charge generation process of $Ir(Ftbpa)_3$:$PC_{71}BM$ blend under photoexcitation. ISC: intersystem crossing; ground state (S_0), lowest singlet state (S_1), lowest triplet state (T_1), singlet charge transfer state (^{1}CT), triplet charge transfer state (^{3}CT), and free charges (FC).

Open Access Article. Published on 30 October 2019. Downloaded on 10/20/2025 7:21:48 PM.
This article is licensed under a Creative Commons Attribution 3.0 Unported Licence.

C–O–C angles and the dihedral angles between the bis(trifluoromethyl)phenyl groups and the benzo[*g*]phthalazine cores are 117° and 86°. Consequently, the bis(trifluoromethyl)phenoxy groups could protect the benzo[*g*]phthalazine moieties and Ir center at one side.

The energy levels of $Ir(Ftbpa)_3$[34] and $Ir(FOtbpa)_3$ were estimated by cyclic voltammogram (CV) measurements (Fig. S1, ESI†). The LUMO/HOMO energy levels of $Ir(Ftbpa)_3$, $Ir(FOtbpa)_3$, and $PC_{71}BM$ are calculated to be −3.04/−5.20, −2.97/−5.13, and −3.75/−5.78 eV (Fig. 1c), respectively. It indicates that insertion of an oxygen-bridge has no obvious effect on the electrochemical LUMO–HOMO gap while both LUMO and HOMO levels are elevated slightly.

To give readers an intuitive understanding of the charge generation process in T-OPVs, the energetic states of the $Ir(Ftbpa)_3$:$PC_{71}BM$ blend is presented in Fig. 1d where the singlet and triplet states of $Ir(Ftbpa)_3$ were calculated in a previous report,[34] and the energies of the CT states is obtained from the FTPS-EQE measurement. In the charge generation process of the singlet system, the CT states are formed directly from the S_1 before being separated into free charges. While in the $Ir(Ftbpa)_3$:$PC_{71}BM$ system, excitons go through a fast ISC from S_1 to T_1 (blue arrow in Fig. 1d). The energy offset between T_1 and ^{3}CT may be beneficial for triplet excitons to form ^{3}CT and then dissociate into free charges (red arrow). However, this is also a possibility even in the triplet system, CT excitons might generate from S_1 without going through T_1 (green line).

The UV-vis absorption spectra of Ftbpa and FOtbpa ligands showed absorption bands below 450 nm (Fig. S2a, ESI†), which could be ascribed to the π–π* transition. Ir complexes, $Ir(Ftbpa)_3$ and $Ir(FOtbpa)_3$, exhibited significantly enhanced and broadened absorption compared to Ftbpa and FOtbpa ligands shown in Fig. 2a. The bands below 450 nm are attributed to the ligands' absorption, while the absorption bands at 450–700 nm correspond to the mixed transitions of ^{1}MLCT (metal-to-ligand charge transfer) and ^{3}MLCT. The weak absorption band extending over 700 nm could be the excitation from the ground states to the lowest triplet state ($S_0 \rightarrow T_1$). After blending with $PC_{71}BM$, the blend films with a weight ratio of 1 : 1.5 showed similar absorption spectra due to the overlapped absorptions between Ir complexes and $PC_{71}BM$. Compared with $Ir(Ftbpa)_3$, $Ir(FOtbpa)_3$ displayed similar NIR phosphorescence with an emission peak at 767 nm, but a lower PL quantum yield (Φ_{PL}) of 10.8% and a shorter phosphorescent lifetime (τ_p) of 489 ns in degassed CH_2Cl_2 (Table S1 and Fig. S2b, ESI†), which are attributed to its slightly enlarged radiative transition rate constant ($k_r = 2.2 \times 10^5\ s^{-1}$) and significantly increased non-radiative transition rate constant ($k_{nr} = 1.8 \times 10^6\ s^{-1}$). The significantly increased k_{nr} of $Ir(FOtbpa)_3$ could be ascribed to the rotation of pendent bis(trifluoromethyl)phenoxy groups in the solution.

In neat films, the $Ir(Ftbpa)_3$ complex showed slightly red-shifted emissions with peaks at 784 nm compared to that of $Ir(FOtbpa)_3$ with peaks at 780 nm (Fig. S2c, ESI†), which should correspond to phosphorescence characteristics of the triplet excited states. Accordingly, the energies of T_1 were estimated, by the highest energy vibronic band of the phosphorescence spectra, to be 1.58 eV and 1.59 eV for $Ir(Ftbpa)_3$ and $Ir(FOtbpa)_3$, respectively. The complete elimination of the ligand fluorescence emissions indicated the strong SOC and efficient ISC rate from S_1 to T_1. The Φ_{PL} of $Ir(FOtbpa)_3$ and $Ir(Ftbpa)_3$ reduced to 2.4% and 2.6% (Table S1, ESI†), respectively, which could be ascribed to the ACQ with enlarged k_{nr} caused by the interactions of triplet excitons such as triplet–triplet annihilation. Also, the τ_p of $Ir(FOtbpa)_3$ and $Ir(Ftbpa)_3$ reduced to 49 ns and 19 ns, respectively (Fig. 2b). The k_{nr} of $Ir(FOtbpa)_3$ and $Ir(Ftbpa)_3$ were calculated to be $2.0 \times 10^7\ s^{-1}$ and $5.1 \times 10^7\ s^{-1}$ in neat films, respectively, which are about 11 times and 43 times larger than their k_{nr} in degassed CH_2Cl_2. The values of k_r were calculated to be $4.9 \times 10^5\ s^{-1}$ and $1.4 \times 10^6\ s^{-1}$ for $Ir(FOtbpa)_3$ and $Ir(Ftbpa)_3$ neat films, respectively. Since the only difference of $Ir(FOtbpa)_3$ and $Ir(Ftbpa)_3$ molecules is the pendent group, the much smaller enhancement of k_{nr} for $Ir(FOtbpa)_3$ is ascribed to the usage of the bis(trifluoromethyl)phenoxy groups as δ-spacers, which hamper the interactions of triplet excitons in aggregated state and alleviate the reductions of Φ_{PL} and τ_p. Thus, $Ir(FOtbpa)_3$ displays longer τ_p in the pristine film, which is beneficial for the exciton diffusion.

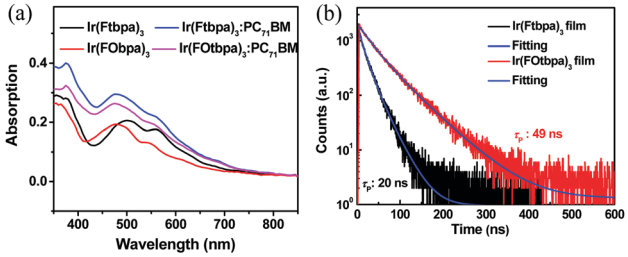

Fig. 2 (a) Absorption spectra of $Ir(Ftbpa)_3$, $Ir(FOtbpa)_3$ and corresponding blend films with $PC_{71}BM$ in a weight ratio of 1 : 1.5; (b) transient PL decay curves of $Ir(Ftbpa)_3$ and $Ir(FOtbpa)_3$ neat films.

To study the voltage losses in T-OPVs, the Ir complexes were evaluated using $PC_{71}BM$ as the electron acceptor with weight ratios of 2 : 1, 1 : 1.5 and 1 : 3. Photovoltaic parameters of the T-OPVs based on $Ir(Ftbpa)_3$ and $Ir(FOtbpa)_3$ are summarized in Table 1. For $Ir(Ftbpa)_3$:$PC_{71}BM$ devices, a PCE of 3.17% with a short-circuit current density (J_{sc}) of 8.70 mA cm^{-2}, V_{oc} of 0.80 V, and fill factor (FF) of 0.46 is obtained at a weight ratio of 1 : 1.5. For $Ir(FOtbpa)_3$:$PC_{71}BM$ devices, the best PCE increases to 3.56% with a V_{oc} of 0.88 V, J_{sc} of 8.58 mA cm^{-2}, and FF of 0.47 at the same weight ratio (1 : 1.5). On the other hand, the Ftbpa and FOtbpa ligands showed very poor performance with low PCEs of 0.001% and 0.007% in similar device structures (Table S2, ESI†), which confirms the significant contribution of Ir to the performance of corresponding T-OPVs. The typical *J*–*V* and EQE curves for Ir complex-based devices with a weight ratio of 1 : 1.5 are shown in Fig. 3a and b. The EQE curves of these Ir complex-based devices showed a spectral response from both donor and acceptor absorption regions (300 to 700 nm). The integrated J_{sc} values from the EQE curves are 8.26 and 8.11 mA cm^{-2} for $Ir(Ftbpa)_3$:$PC_{71}BM$ and $Ir(FOtbpa)_3$:$PC_{71}BM$ devices, respectively, which are consistent with the values from *J*–*V* measurement. The *J*–*V* characteristics of the hole-only and electron-only devices are shown in Fig. S3a and b (ESI†).

Open Access Article. Published on 30 October 2019. Downloaded on 10/20/2025 7:21:48 PM.
This article is licensed under a Creative Commons Attribution 3.0 Unported Licence.

Table 1 Summary of photovoltaic parameters of T-OPVs based on $Ir(Ftbpa)_3$ and $Ir(FOtbpa)_3$ with different ratios. The average values were obtained from over 20 devices

Donor	Ratio	V_{oc} (V)	J_{sc} (mA cm^{-2})	FF	PCE (%)
$Ir(Ftbpa)_3$	2 : 1	0.85 (0.85 ± 0.01)	6.43 (6.47 ± 0.1)	0.39 (0.38 ± 0.01)	2.13 (2.07 ± 0.19)
	1 : 1.5	0.80 (0.80 ± 0.01)	8.70 (8.72 ± 0.19)	0.46 (0.43 ± 0.02)	3.17 (3.01 ± 0.19)
	1 : 3	0.78 (0.78 ± 0.01)	8.62 (8.58 ± 0.07)	0.42 (0.41 ± 0.01)	2.97 (2.71 ± 0.05)
$Ir(FOtbpa)_3$	2 : 1	0.93 (0.93 ± 0.01)	5.07 (4.67 ± 0.23)	0.32 (0.31 ± 0.01)	1.51 (1.34 ± 0.09)
	1 : 1.5	0.88 (0.88 ± 0.01)	8.58 (8.41 ± 0.51)	0.47 (0.45 ± 0.02)	3.56 (3.30 ± 0.26)
	1 : 3	0.85 (0.85 ± 0.02)	8.11 (8.14 ± 0.44)	0.46 (0.41 ± 0.03)	3.15 (2.80 ± 0.23)

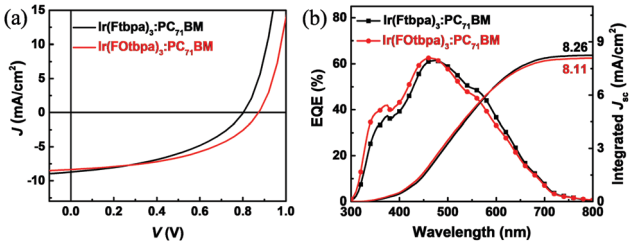

Fig. 3 (a) J–V characteristics of the T-OPVs based on $Ir(Ftbpa)_3:PC_{71}BM$ and $Ir(FOtbpa)_3:PC_{71}BM$ blends with a weight ratio of 1 : 1.5; (b) EQE and integrated J_{sc} of $Ir(Ftbpa)_3:PC_{71}BM$ and $Ir(FOtbpa)_3:PC_{71}BM$ blends with a weight ratio of 1 : 1.5.

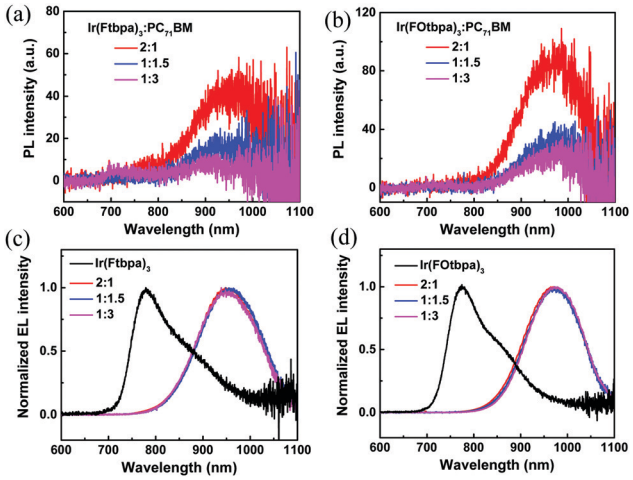

Fig. 4 Sub-band-gap PL spectra from CT transitions of (a) $Ir(Ftbpa)_3:PC_{71}BM$ and (b) $Ir(FOtbpa)_3:PC_{71}BM$ blends with different weight ratios. The films were excited by a 532 nm laser; (c) EL spectra for pristine $Ir(Ftbpa)_3$ and $Ir(Ftbpa)_3$:$PC_{71}BM$ blends with different weight ratios; (d) the EL spectra of pristine $Ir(FOtbpa)_3$ and $Ir(FOtbpa)_3:PC_{71}BM$ blends with different weight ratios.

The hole and electron mobilities are 6.6×10^{-7} and 1.76×10^{-4} cm^2 V^{-1} s^{-1} for $Ir(Ftbpa)_3$ blends (ratio 1 : 1.5) and 1.5×10^{-6} and 1.5×10^{-4} cm^2 V^{-1} s^{-1} for $Ir(FOtbpa)_3$ blends (ratio 1 : 1.5), as found through the SCLC measurements. The lower hole mobilities than the singlet materials resulted in unbalanced mobilities and the smaller FFs here.

Comparing the devices based on these two Ir complexes with different weight ratios, we find that the V_{oc} increases with increasing content of the Ir complexes. Similar phenomena have been reported and attributed to the changes in the interfacial area of the donor/acceptor.[17,37] Atomic force microscopy (AFM) was used to investigate the morphologies of the blend films with different weight ratios. As shown in the images (Fig. S4, ESI†), there seem to be minor morphological differences between the different blend ratios for both $Ir(Ftbpa)_3$:$PC_{71}BM$ and $Ir(FOtbpa)_3$:$PC_{71}BM$ blend films. While AFM only examines the surface morphology, the phase separation of the whole active layer could be investigated by PL measurement. Steady state PL spectra of the pristine $Ir(Ftbpa)_3$ and $Ir(FOtbpa)_3$ films are compared with their corresponding blends with different weight ratios (Fig. S5, ESI†). The PL intensities from $Ir(Ftbpa)_3$ and $Ir(FOtbpa)_3$ triplet excitons are strongly quenched by $PC_{71}BM$ in all blends, indicating efficient excitons dissociation and charge transfer between the two Ir complex donors and $PC_{71}BM$ acceptor with highly mixed donors and acceptors. The CT state PL from 2 : 1, 1 : 1.5, and 1 : 3 $Ir(Ftbpa)_3:PC_{71}BM$ blend films are presented in Fig. 4a. The interfacial CT state emission is observed at ~950 nm, which is clearly red-shifted compared to $Ir(Ftbpa)_3$ exciton emission at 784 nm. Furthermore, it shows a clear trend of suppressed CT PL from the films with a higher $PC_{71}BM$ content. Similar results have also been found in $Ir(FOtbpa)_3$:$PC_{71}BM$ blends (Fig. 4b). Since the CT PL intensities are generally very low, EL measurement is a much more sensitive method to determine the E_{CT}. Therefore, the EL emission from devices based on pristine Ir complexes and their blends are also recorded. As shown in Fig. 4c and d, these electrically generated CT state EL emissions are consistent with the CT state PL emissions generated by photoexcitation. The $Ir(Ftbpa)_3$:$PC_{71}BM$ blend films showed red-shift EL emissions at around 950 nm compared to 780 nm for the pristine $Ir(Ftbpa)_3$ devices (Fig. 4c). Similar red-shift EL emissions are observed in the $Ir(FOtbpa)_3$:$PC_{71}BM$ blends (Fig. 4d) at around 973 nm. These indicate that the triplet energy of $Ir(Ftbpa)_3$ and $Ir(FOtbpa)_3$ are much higher than the E_{CT} in the blends, which confirms the effective utilization of triplet excitons in the charge generation process.

More specifically, the E_{CT} can be determined through fitting the FTPS-EQE spectra according to the model developed by Vandewal based on Marcus theory.

$$\mathrm{EQE_{PV}}(E) = \frac{f}{E\sqrt{4\pi\lambda KT}}\exp\left(\frac{-(E_{CT}+\lambda-E)^2}{4\lambda KT}\right) \quad (2)$$

where f is proportional to the absorption strength of the CT state, K is the Boltzmann's constant, T is the absolute temperature and λ is the reorganization energy. FTPS-EQE spectra and corresponding fits by eqn (2) of these two Ir complex blends are

Open Access Article. Published on 30 October 2019. Downloaded on 10/20/2025 7:21:48 PM.
This article is licensed under a Creative Commons Attribution 3.0 Unported Licence.

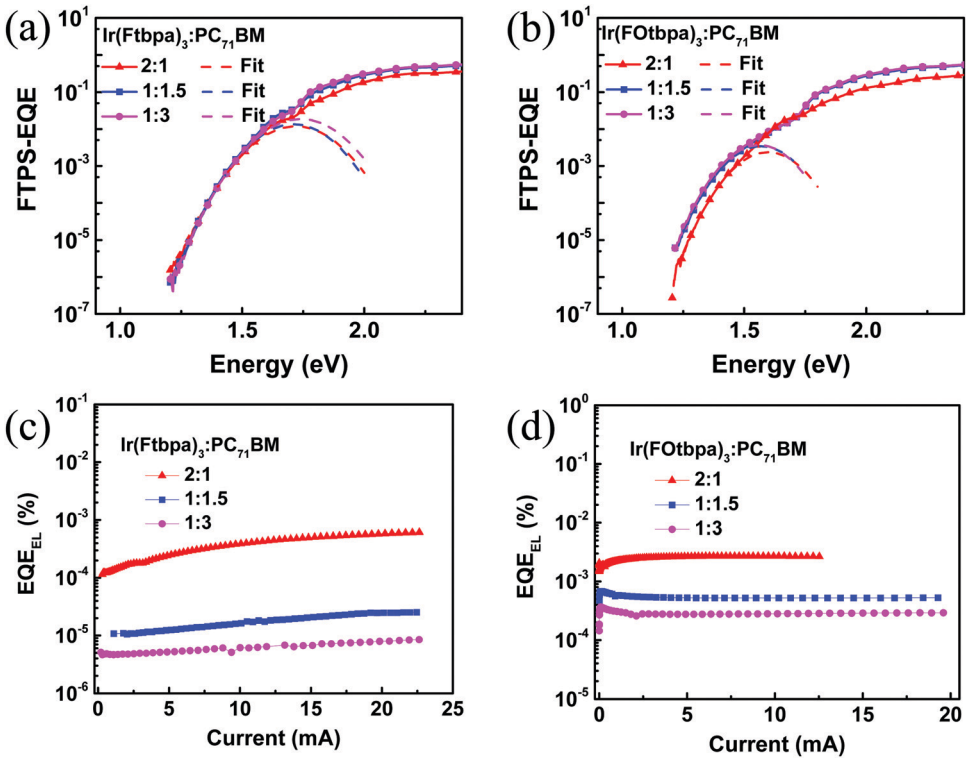

Fig. 5 FTPS-EQE spectra of (a) Ir(Ftbpa)$_3$:PC$_{71}$BM and (b) Ir(FOtbpa)$_3$:PC$_{71}$BM. The dash curves are fits of the FTPS-EQE spectra using eqn (2); (c) EQE$_{EL}$ of the Ir(Ftbpa)$_3$:PC$_{71}$BM and (d) Ir(FOtbpa)$_3$:PC$_{71}$BM.

shown in Fig. 5a and b, respectively. For the Ir(Ftbpa)$_3$-based devices, E_{CT} values of 1.46 eV, 1.47 eV, and 1.48 eV are obtained for the 2 : 1, 1 : 1.5, and 1 : 3 blends. For the Ir(FOtbpa)$_3$-based devices, E_{CT} values of 1.41 eV, 1.38 eV, and 1.38 eV are obtained for the 2 : 1, 1 : 1.5, and 1 : 3 blends.

As shown in Table 1, the V_{oc} of the OPVs based on Ir(Ftbpa)$_3$ are in the range of 0.85–0.78 V and the V_{oc} of the OPVs based on Ir(FOtbpa)$_3$ are in the range of 0.93–0.85 V. The contradiction between E_{CT} and V_{oc} for different blend ratios motivates us to further understand the voltage losses. Considering the detailed balance theory, the V_{oc} of OPVs is then determined by eqn (3), where radiative ($q\Delta V_{rad}$) and non-radiative ($q\Delta V_{non\text{-}rad}$) recombination losses can be experimentally determined by the fitting parameters and measured EQE$_{EL}$.

$$V_{oc} = \frac{E_{CT}}{q} - q\Delta V_{rad} - q\Delta V_{non\text{-}rad} = \frac{E_{CT}}{q} + KT\ln\left(\frac{J_{SC}h^3c^2}{fq2\pi(E_{CT}-\lambda)}\right) + kT\,\mathrm{In}(\mathrm{EQE_{EL}}) \quad (3)$$

where EQE$_{EL}$ is the external quantum efficiency of the EL of the device.

The $q\Delta V_{rad}$ and $q\Delta V_{non\text{-}rad}$ for blends with different ratios were calculated (Table 2). The $q\Delta V_{rad}$ for both Ir(Ftbpa)$_3$ and Ir(FOtbpa)$_3$-based devices is independent with blend ratios. From the EQE$_{EL}$ measurements (Fig. 5c, d and Table 2), the EQE$_{EL}$ of the Ir(Ftbpa)$_3$ and Ir(FOtbpa)$_3$-based devices decreased with increasing content of PC$_{71}$BM. These lead to low $q\Delta V_{non\text{-}rad}$ for both Ir(Ftbpa)$_3$ and Ir(FOtbpa)$_3$-based devices resulting in a higher V_{oc} with a low PC$_{71}$BM content.

For the best device performances based on Ir(Ftbpa)$_3$ and Ir(FOtbpa)$_3$ blends (1 : 1.5), as shown in Table 1, the difference in the PCEs is mainly due to the difference in V_{oc}s. When we compare the energy levels of these two donors, the HOMO level of Ir(Ftbpa)$_3$ is lower than that of Ir(FOtbpa)$_3$ (Fig. 1b), which indicates that the Ir(Ftbpa)$_3$ blend may have a higher V_{oc}. However, the V_{oc} of Ir(Ftbpa)$_3$-based devices is 0.08 V lower than that of the Ir(FOtbpa)$_3$-based devices. The Ir(Ftbpa)$_3$-based devices have a higher E_{CT} of 1.47 eV compared with the value of 1.38 eV for the Ir(FOtbpa)$_3$-based devices, which is consistent

Table 2 Summary of fitting parameters and calculated $q\Delta V_{rad}$ and $q\Delta V_{non\text{-}rad}$ values for T-OPVs

Donor	Ratio	qV_{oc} (eV)	f_1 (eV^2)	E_{CT} (eV)	λ (eV)	$q\Delta V_{rad}$ (eV)	EQE$_{EL}$ (%)	$q\Delta V_{non\text{-}rad}$ (eV)
Ir(Ftbpa)$_3$	2 : 1	0.85	6×10^{-3}	1.46	0.27	0.25	1×10^{-4}	0.36
	1 : 1.5	0.80	6×10^{-3}	1.47	0.25	0.25	1×10^{-5}	0.42
	1 : 3	0.78	9×10^{-3}	1.48	0.27	0.26	5×10^{-6}	0.44
Ir(FOtbpa)$_3$	2 : 1	0.93	9×10^{-4}	1.41	0.19	0.21	2×10^{-3}	0.27
	1 : 1.5	0.88	6×10^{-4}	1.38	0.12	0.19	7×10^{-4}	0.31
	1 : 3	0.85	1×10^{-3}	1.38	0.18	0.20	3×10^{-4}	0.33

 This journal is © The Royal Society of Chemistry 2019

Open Access Article. Published on 30 October 2019. Downloaded on 10/20/2025 7:21:48 PM.
This article is licensed under a Creative Commons Attribution 3.0 Unported Licence.

with the HOMO level difference. The $q\Delta V_{rad}$ for Ir(Ftbpa)$_3$-based devices is 0.25 eV, which is higher than the value of 0.19 eV for the Ir(FOtbpa)$_3$-based devices. The EQE_{EL} of the device based on Ir(FOtbpa)$_3$ is more than one order of magnitude higher than that of the Ir(Ftbpa)$_3$. This leads to a calculated $q\Delta V_{non\text{-}rad}$ of 0.31 eV for the Ir(FOtbpa)$_3$-based devices, about 0.11 eV lower than that of the Ir(Ftbpa)$_3$-based devices. Both radiative and non-radiative recombinations for the Ir(FOtbpa)$_3$-based devices are lower than those of the Ir(Ftbpa)$_3$-based devices, which results in a higher V_{oc} for the Ir(FOtbpa)$_3$-based devices. The calculated data fit well with V_{oc} in these two blends.

Contradictory to the energy gap law (the non-radiative decay rate is exponentially increasing with decreasing energy difference between the excited and ground states), the Ir(FOtbpa)$_3$-based device has a lower E_{CT}, but a higher EQE_{EL}. Considering the photophysical properties of the two Ir complexes, the larger k_r (1.4×10^6 s^{-1}) of Ir(Ftbpa)$_3$ than that of Ir(FOtbpa)$_3$ ($k_r = 4.9 \times 10^5$ s^{-1}) in solid state may correlate with the larger radiative recombination loss in Ir(Ftbpa)$_3$-based devices. The longer exciton lifetime (τ = 49 ns) and much smaller k_{nr} (2.0×10^7 s^{-1}) compared with those of Ir(Ftbpa)$_3$ (τ = 19 ns and $k_{nr} = 5.1 \times 10^7$ s^{-1}) in pristine films due to the flexible inert δ-spacer may decrease the non-radiative recombination loss in Ir(FOtbpa)$_3$-based devices. In addition to the above reasons, some other charge carrier loss mechanisms may coexist in the Ir(Ftbpa)$_3$-based devices.

The recombination mechanism was further studied by measuring the light intensity dependencies of J_{sc} and V_{oc} (Fig. S6, ESI†). The Ir(Ftbpa)$_3$ and Ir(FOtbpa)$_3$-based devices (1 : 1.5) show figure-of-merit (α) values of 0.93 and 0.92, respectively, indicating that bimolecular recombination occurs in both systems at short circuit conditions. At open circuit conditions, a slope of 2 k_{BT}/q for monomolecular (trap-assisted) recombination and a slope of 1 k_{BT}/q for bimolecular recombination exist. In some cases, surface recombination would make the slope less than 1 k_{BT}/q. The Ir(FOtbpa)$_3$-based devices (1 : 1.5) show a slope of 1.03 k_{BT}/q, while the Ir(Ftbpa)$_3$-based devices (1 : 1.5) show a slope less than 1 k_{BT}/q (0.95 k_{BT}/q). Thus, the Ir(Ftbpa)$_3$-based devices (1 : 1.5) is more dominated by surface recombination than the Ir(FOtbpa)$_3$-based devices (1 : 1.5), which is consistent with the non-radiative recombination losses from EQE_{EL} calculations.

Conclusions

In summary, the voltage losses in T-OPVs based on two Ir complexes and $PC_{71}BM$ are studied from the aspects of radiative and non-radiative recombination. Firstly, significantly increased PCE from 0.007% (devices based on ligands) to 3.56% (the Ir(FOtbpa)$_3$-based devices) was observed, which confirms the major contribution by introducing Ir. Secondly, a trend of increasing V_{oc} with increasing donor contents was found in two Ir complex systems by varying the weight ratios between the donors and acceptors. Thirdly, T-OPVs based on Ir(FOtbpa)$_3$ exhibited a higher V_{oc} compared to Ir(Ftbpa)$_3$, which could be attributed to supressed non-radiative recombination losses due to the relatively small k_{nr} for Ir(FOtbpa)$_3$. Furthermore, the additional surface recombination in the Ir(Ftbpa)$_3$-based devices also has an impact on the non-radiative recombination losses, which results in a lower V_{oc}.

Conflicts of interest

There are no conflicts to declare.

Acknowledgements

F. Zhang and Y. Jin acknowledge funding from the Swedish Foundation for International Cooperation in Research and Higher Education (STINT) for the Joint China-Sweden Mobility programme, the Knut and Alice Wallenberg foundation under contract 2016.0059, the Swedish Government Research Area in Materials Science on Functional Materials at Linköping University (Faculty Grant SFO-Mat-LiU No. 200900971) and the China Scholarship Council (CSC). J. Qiao would like to thank the financial support from the NSFC of China (51711530040 and 51473086). J. Xue thanks the National Postdoctoral Program for Innovative Talents (BX20180159) for the financial support.

References

1 J. Yuan, Y. Zhang, L. Zhou, G. Zhang, H.-L. Yip, T.-K. Lau, X. Lu, C. Zhu, H. Peng, P. A. Johnson, M. Leclerc, Y. Cao, J. Ulanski, Y. Li and Y. Zou, *Joule*, 2019, **3**, 1140–1151.
2 B. Fan, D. Zhang, M. Li, W. Zhong, Z. Zeng, L. Ying, F. Huang and Y. Cao, *Sci. China: Chem.*, 2019, **62**, 746–752.
3 K. Vandewal, K. Tvingstedt, A. Gadisa, O. Inganäs and J. V. Manca, *Phys. Rev. B: Condens. Matter Mater. Phys.*, 2010, **81**, 125204.
4 M. C. Scharber, D. Mühlbacher, M. Koppe, P. Denk, C. Waldauf, A. J. Heeger and C. J. Brabec, *Adv. Mater.*, 2006, **18**, 789–794.
5 J. Widmer, M. Tietze, K. Leo and M. Riede, *Adv. Funct. Mater.*, 2013, **23**, 5814–5821.
6 K. Kawashima, Y. Tamai, H. Ohkita, I. Osaka and K. Takimiya, *Nat. Commun.*, 2015, **6**, 10085.
7 H.-Y. Chen, J. Hou, S. Zhang, Y. Liang, G. Yang, Y. Yang, L. Yu, Y. Wu and G. Li, *Nat. Photonics*, 2009, **3**, 649.
8 S. Albrecht, S. Janietz, W. Schindler, J. Frisch, J. Kurpiers, J. Kniepert, S. Inal, P. Pingel, K. Fostiropoulos, N. Koch and D. Neher, *J. Am. Chem. Soc.*, 2012, **134**, 14932–14944.
9 W. Li, K. H. Hendriks, A. Furlan, M. M. Wienk and R. A. J. Janssen, *J. Am. Chem. Soc.*, 2015, **137**, 2231–2234.
10 K. Vandewal, Z. Ma, J. Bergqvist, Z. Tang, E. Wang, P. Henriksson, K. Tvingstedt, M. R. Andersson, F. Zhang and O. Inganäs, *Adv. Funct. Mater.*, 2012, **22**, 3480–3490.
11 J. Liu, S. Chen, D. Qian, B. Gautam, G. Yang, J. Zhao, J. Bergqvist, F. Zhang, W. Ma, H. Ade, O. Inganäs, K. Gundogdu, F. Gao and H. Yan, *Nat. Energy*, 2016, **1**, 16089.
12 S. Li, L. Zhan, C. Sun, H. Zhu, G. Zhou, W. Yang, M. Shi, C.-Z. Li, J. Hou, Y. Li and H. Chen, *J. Am. Chem. Soc.*, 2019, **141**, 3073–3082.

Open Access Article. Published on 30 October 2019. Downloaded on 10/20/2025 7:21:48 PM.
This article is licensed under a Creative Commons Attribution 3.0 Unported Licence.

13 S. Chen, Y. Wang, L. Zhang, J. Zhao, Y. Chen, D. Zhu, H. Yao, G. Zhang, W. Ma, R. H. Friend, P. C. Y. Chow, F. Gao and H. Yan, *Adv. Mater.*, 2018, **30**, 1804215.
14 H. Fu, Y. Wang, D. Meng, Z. Ma, Y. Li, F. Gao, Z. Wang and Y. Sun, *ACS Energy Lett.*, 2018, **3**, 2729–2735.
15 Z. Tang, J. Wang, A. Melianas, Y. Wu, R. Kroon, W. Li, W. Ma, M. R. Andersson, Z. Ma, W. Cai, W. Tress and O. Inganäs, *J. Mater. Chem. A*, 2018, **6**, 12574–12581.
16 J. Benduhn, K. Tvingstedt, F. Piersimoni, S. Ullbrich, Y. Fan, M. Tropiano, K. A. McGarry, O. Zeika, M. K. Riede, C. J. Douglas, S. Barlow, S. R. Marder, D. Neher, D. Spoltore and K. Vandewal, *Nat. Energy*, 2017, **2**, 17053.
17 K. Vandewal, J. Widmer, T. Heumueller, C. J. Brabec, M. D. McGehee, K. Leo, M. Riede and A. Salleo, *Adv. Mater.*, 2014, **26**, 3839–3843.
18 D. Qian, Z. Zheng, H. Yao, W. Tress, T. R. Hopper, S. Chen, S. Li, J. Liu, S. Chen, J. Zhang, X.-K. Liu, B. Gao, L. Ouyang, Y. Jin, G. Pozina, I. A. Buyanova, W. M. Chen, O. Inganäs, V. Coropceanu, J.-L. Bredas, H. Yan, J. Hou, F. Zhang, A. A. Bakulin and F. Gao, *Nat. Mater.*, 2018, **17**, 703–709.
19 X. Liu, X. Du, J. Wang, C. Duan, X. Tang, T. Heumueller, G. Liu, Y. Li, Z. Wang, J. Wang, F. Liu, N. Li, C. J. Brabec, F. Huang and Y. Cao, *Adv. Energy Mater.*, 2018, **8**, 1801699.
20 P. Heremans, D. Cheyns and B. P. Rand, *Acc. Chem. Res.*, 2009, **42**, 1740–1747.
21 O. V. Mikhnenko, R. Ruiter, P. W. M. Blom and M. A. Loi, *Phys. Rev. Lett.*, 2012, **108**, 137401.
22 Z. Xu, B. Hu and J. Howe, *J. Appl. Phys.*, 2008, **103**, 043909.
23 M. B. Smith and J. Michl, *Chem. Rev.*, 2010, **110**, 6891–6936.
24 D. N. Congreve, J. Lee, N. J. Thompson, E. Hontz, S. R. Yost, P. D. Reusswig, M. E. Bahlke, S. Reineke, T. Van Voorhis and M. A. Baldo, *Science*, 2013, **340**, 334–337.
25 H. Zhen, Q. Hou, K. Li, Z. Ma, S. Fabiano, F. Gao and F. Zhang, *J. Mater. Chem. A*, 2014, **2**, 12390–12396.
26 M. H. Yun, E. Lee, W. Lee, H. Choi, B. R. Lee, M. H. Song, J.-I. Hong, T.-H. Kwon and J. Y. Kim, *J. Mater. Chem. C*, 2014, **2**, 10195–10200.
27 M. Qian, R. Zhang, J. Hao, W. Zhang, Q. Zhang, J. Wang, Y. Tao, S. Chen, J. Fang and W. Huang, *Adv. Mater.*, 2015, **27**, 3546–3552.
28 Y.-N. Liu, S.-F. Wang, Y.-T. Tao and W. Huang, *Chin. Chem. Lett.*, 2016, **27**, 1250–1258.
29 I. A. Wright, *Polyhedron*, 2018, **140**, 84–98.
30 L. Xu, C.-L. Ho, L. Liu and W.-Y. Wong, *Coord. Chem. Rev.*, 2018, **373**, 233–257.
31 Y. Jin, Y. Zhang, Y. Liu, J. Xue, W. Li, J. Qiao and F. Zhang, *Adv. Mater.*, 2019, **31**, 1900690.
32 Q. Wu, Y. Cheng, Z. Xue, X. Gao, M. Wang, W. Yuan, S. Huettner, S. Wan, X. Cao, Y. Tao and W. Huang, *Chem. Commun.*, 2019, **55**, 2640–2643.
33 J. Benduhn, F. Piersimoni, G. Londi, A. Kirch, J. Widmer, C. Koerner, D. Beljonne, D. Neher, D. Spoltore and K. Vandewal, *Adv. Energy Mater.*, 2018, **8**, 1800451.
34 J. Xue, L. Xin, J. Hou, L. Duan, R. Wang, Y. Wei and J. Qiao, *Chem. Mater.*, 2017, **29**, 4775–4782.
35 P. N. Murgatroyd, *J. Phys. D: Appl. Phys.*, 1970, **3**, 151–156.
36 N. Felekidis, A. Melianas and M. Kemerink, *Org. Electron.*, 2018, **61**, 318–328.
37 Z. He, B. Xiao, F. Liu, H. Wu, Y. Yang, S. Xiao, C. Wang, T. P. Russell and Y. Cao, *Nat. Photonics*, 2015, **9**, 174.

 This journal is © The Royal Society of Chemistry 2019